

Ab-initio investigation of Br-3d core-excited electronic structures of HBr and HBr⁺

Yuki Kobayashi,¹ Tao Zeng,^{2, a)} Daniel M. Neumark,^{1, 3, b)} and Stephen R. Leone^{1, 4, 5, c)}

¹⁾*Department of Chemistry, University of California, Berkeley, California 94720, USA*

²⁾*Department of Chemistry, Carleton University, Ottawa, Ontario K1S5B6, Canada*

³⁾*Chemical Sciences Division, Lawrence Berkeley National Laboratory, Berkeley, CA 94720, USA*

⁴⁾*Chemical Sciences Division, Lawrence Berkeley National Laboratory, Berkeley, California 94720, USA*

⁵⁾*Department of Physics, University of California, Berkeley, California 94720, USA*

(Dated: 24 February 2020)

Ultrafast X-ray absorption spectroscopy is a powerful tool for real-time probing of chemical dynamics. Interpretation of the time-resolved absorption spectra requires knowledge of core-excited potentials, which necessitates assistance from high-level electronic-structure computations. In this study, we investigate Br-3d core-excited electronic structures of hydrogen bromide (HBr) using the spin-orbit general multiconfigurational quasidegenerate perturbation theory (SO-GMC-QDPT). Core-to-valence excitation energies and transition dipole moments are computed as functions of the internuclear distance for five electronic states of HBr ($^1\Sigma_0^+$, $^3\Pi_1$, $^1\Pi_1$, $^3\Pi_0^+$, $^3\Pi_1$) and two electronic states of HBr⁺ ($^2\Pi_{3/2}$, $^2\Sigma_{1/2}$). The results illustrate the capabilities of the Br-3d edge probing to capture transitions of electronic-state symmetry as well as nonadiabatic dissociation processes evolving across avoided crossings. Furthermore, core-to-valence absorption spectra are simulated from the neutral and ionic ground states by numerically solving the time-dependent Schrödinger equation, which exhibit an excellent agreement with an experimental spectrum. The calculated comprehensive and quantitative picture of the core-excited potentials allows for transparent analyses of the core-to-valence absorption signals, filling the gap in the theoretical understanding of the Br-3d absorption spectra.

I. INTRODUCTION

X-ray absorption spectroscopy is a powerful tool to study chemical dynamics from gas-phase molecules to solid-state materials^{1,2}. Subtle changes in electronic states are reflected in the spectral shape, giving X-ray absorption spectroscopy unique capabilities to resolve charge-state, spin-state, and structural information of target systems. Recent developments in the wavelength-up-conversion technique through high-harmonic generation (HHG)³ have improved the time resolution of the X-ray light sources from tens of femtoseconds to hundreds of attoseconds⁴⁻⁶. The past decade has witnessed a great success of X-ray absorption spectroscopy in real-time tracking of ultrafast chemical dynamics. Examples include electronic coherence dynamics in rare-gas atoms^{7,8}, photodissociation or multi-mode vibrations of gas-phase molecules⁹⁻¹⁴, and charge-carrier dynamics of solid state materials¹⁵⁻¹⁸.

Interpretation of time-resolved X-ray absorption spectra requires a comprehensive picture of potential energy surfaces both in valence and core-excited states. Experimental characterization of the core-excited landscapes is difficult due to the inherently short autoionization life-

times. Theoretical calculations, therefore, are needed to predict and explain the transitions, but there are several challenges in the computational treatment of core-excited states¹⁹. First, core-excited states are embedded in an energy-level continuum lying above an ionization threshold. A reduction of the number of configuration state functions to a tractable extent is necessary. Second, for core electrons, especially the ones in heavy elements, relativistic effects such as spin-orbit coupling play significant roles. Third, calculations have to be robust throughout the entire reaction coordinates, from Franck-Condon region through transient states to asymptotic limits. As ultrafast X-ray absorption spectroscopy is becoming a standard technique, computational tools that can be widely applied for core-excited states are strongly desired²⁰⁻²².

Here we employ computational chemistry methods to study the Br-3d core-excited states in hydrogen bromide (HBr). The Br-3d edge exhibits characteristic absorption peaks in the photon-energy region from 60 eV to 75 eV²³, which are readily accessible using HHG-based attosecond extreme ultraviolet (XUV) light sources. A series of experiments have been reported on the Br-3d edge probing of molecular dynamics^{9,24-27}. Challenges lie on the computational side: first, spin-orbit coupling becomes significant for the heavy Br atom, both for the 4p-valence and 3d-core orbitals; second, the ten-fold degeneracy of the 3d orbitals in the M shell yields a larger number of core-excited configurations compared to the s or p orbitals in the inner K and L shells, which become more relevant in the soft and hard X-ray regime. The target molecule HBr

^{a)}Electronic mail: TobyZeng@cunet.carleton.ca

^{b)}Electronic mail: dneumark@berkeley.edu

^{c)}Electronic mail: srl@berkeley.edu

serves as a benchmark for numerous spectroscopic studies for its simple structure and rich photoexcited dynamics. The UV photolysis of HBr involves multiple electronic states, which become spectroscopically bright due to intensity borrowing induced by spin-orbit coupling^{28–30}. In the ionic HBr⁺, the ground bound state exhibits a doublet structure due to spin-orbit splitting^{31,32}. Spectroscopic studies have also characterized predissociation in the ionic excited state, and a set of rotational and vibrational constants have been measured^{33–36}.

The Br-3*d* core-to-valence absorption signals are calculated using the recently developed method of spin-orbit general multiconfigurational quasidegenerate perturbation theory (SO-GMC-QDPT)³⁷. The computed results allow for a transparent analysis of the Br-3*d* edge probing of photoexcited dynamics, which is performed for the first time in this work. Section II of the paper describes computational details. Sections III and IV discuss the computed valence and core-excited electronic structures of HBr and HBr⁺, respectively. Section V compares the simulated Br-3*d* core-to-valence absorption spectrum to an experimental transient absorption spectrum. Finally, Section VI provides the conclusions.

II. COMPUTATIONAL DETAILS

The electronic structure of HBr is computed using the SO-GMC-QDPT code^{37–40} implemented in the developer version of the GAMESS-US program package⁴¹. In all computations, the ZFK-DK3 relativistic model core potentials (MCP) and basis sets of triple-zeta quality^{42–45} are used. The MCPs are optimized to reproduce the integrals related to spin-orbit couplings, and they remove 12 core electrons from the Br atom. In the perturbation-treatment step, an energy denominator shift of 0.01 Hartree is applied for intruder state avoidance^{46,47}.

A Hartree-Fock self-consistent field (SCF) computation is performed at the ground-state equilibrium internuclear distance $R_e = 1.41$ Å. The resultant molecular orbitals are used as initial orbitals for the subsequent state-averaged multi-configurational self-consistent field method (SA-MCSCF) computations. Two active spaces are constructed based on the occupation restricted multiple active space (ORMAS) scheme. The valence-active space is composed of the Br-4*p* and H-1*s* orbitals, containing 6 electrons in 4 orbitals (or 5 electrons in the ionic case). This is a complete active space. The core-active space is composed of the Br-3*d* orbitals, and it is fully occupied containing 10 electrons in 5 orbitals. Single excitations from the core to the valence-active space are allowed, giving the targeted core-to-valence excitations.

The valence electronic structures are computed using the valence-active space alone, and the core-excited electronic structures are computed using both the valence- and core-active spaces. The five Br-3*d* orbitals are frozen in the SA-MCSCF step to facilitate convergence. In order to obtain the correct spin-orbit energy splittings (3685

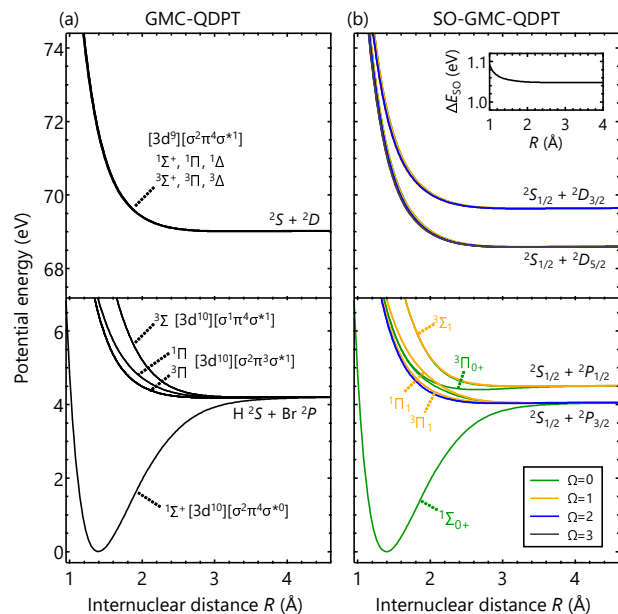


FIG. 1. Potential energy curves of HBr as a function of the internuclear distance R obtained from calculations (a) without and (b) with spin-orbit coupling. The lower panels show the valence states, and the upper panels show the Br-3*d* core-excited states. For the spin-orbit-coupled states, different colors are used for states with different Ω quantum numbers. The inset in (b) shows the averaged energy difference between the $^2D_{5/2-}$ and $^2D_{3/2-}$ -associated states along the dissociation.

cm^{-1} for Br-4*p*, and 8388 cm^{-1} for Br-3*d* orbitals⁴⁸), the effective-nuclear charges $Z_{\text{eff}} = 35.9$ and 39.3 are used for Br in the valence- and the core-excited-states calculations, respectively. The potential energy curves of the neutral (ionic) core-excited states are shifted upward by 1.01 (1.11) eV with respect to those of the valence states, so that the experimental 3*d* \rightarrow 4*p* excitation energies in Br atom (cation) are reproduced²³.

III. NEUTRAL ELECTRONIC STATES

In this section, we present the computed results for the HBr molecule. Firstly, electronic structures of the valence and core-excited states are analyzed. Then, the core-to-valence absorption signals relevant to the UV photolysis are discussed.

A. Valence states

Figures 1(a) and (b) show spin-orbit-free and spin-orbit-coupled potential energy curves of HBr, respectively. Molecular term symbols $^S\Lambda_\Omega$ are assigned based on the main compositions of the states at $R = 1.4$ Å. Atomic-state labels $^S P_J$ are also given for the asymptotic limits.

State	R_e (Å)	ω_e (cm ⁻¹)	$\omega_e x_e$ (cm ⁻¹)	Ref.	
HBr	$X^1\Sigma_0^+$	1.40	2652.5	48.1	<i>a</i>
		1.41	2649.0	45.2	<i>b, d</i>
HBr ⁺	$X^2\Pi_{3/2}$	1.45	2345.4	42.6	<i>a</i>
		1.45	2439.0	45.2	<i>b, d</i>
	$X^2\Pi_{1/2}$	1.45	2343.3	43.0	<i>a</i>
		1.45	2431.3	44.0	<i>b, d</i>
	$A^2\Sigma_{1/2}$	1.68	1336.4	32.4	<i>a</i>
HBr ^{*+}	$^2\Delta_{5/2}$	1.44	2400.0	45.7	<i>a</i>
		1.44	2403.4	46.8	<i>a</i>
	$^2\Pi_{3/2}$	1.44	2410.7	48.4	<i>a</i>
	$^2\Sigma_{1/2}$	1.44	2401.2	46.5	<i>a</i>
	$^2\Delta_{3/2}$	1.44	2401.2	46.5	<i>a</i>
	$^2\Pi_{1/2}$	1.44	2413.5	48.5	<i>a</i>

TABLE I. Spectroscopic parameters determined for the bound electronic states in HBr and HBr⁺. Reference values are taken from previous experimental works. *a*: this work. *b*: ω_e and $\omega_e x_e$ taken from Ref. 50. *c*: ω_e and $\omega_e x_e$ from Ref. 34, converted by the authors. *d*: R_e taken from Ref. 32.

The valence states of HBr (lower panels in Figure 1) arising from the H (2S)+Br (2P) asymptote have already been well documented^{29,30}, and a brief summary is as follows. The bonding σ orbital and the anti-bonding σ^* orbital consist of the Br-4 p_z and the H-1 s orbitals, and the non-bonding π orbitals are nearly identical to the atomic Br-4 $p_{x,y}$ orbitals. The H (2S)+Br (2P) asymptote gives rise to four molecular states in the lowest valence structure, $^1\Sigma^+$, $^3\Sigma^+$, $^1\Pi$, and $^3\Pi$. The strong spin-orbit coupling in the Br-4 p orbitals causes splitting and mixing of the electronic states. The atomic 2P states are split into the upper $^2P_{1/2}$ and the lower $^2P_{3/2}$ states ($\Delta E_{SO} = 0.46$ eV)²³. The singlet and triplet state-mixing by spin-orbit coupling causes more valence electronic states to be populated in the UV excitation through intensity borrowing. Dipole transitions from the ground $^1\Sigma_0^+$ state are allowed into the states with $\Omega = 0^+, 1$, namely, $^1\Pi_1$, $^3\Pi_0^+$, $^3\Pi_1$, and $^3\Sigma_1$, while without spin-orbit coupling, only the $^1\Pi$ state would be populated. Among those spectroscopically bright states, the $^3\Pi_1$ and $^1\Pi_1$ states correlate with the lower $^2P_{3/2}$ asymptote, whereas the $^3\Pi_0^+$ and $^3\Sigma_1$ states correlate with the upper $^2P_{1/2}$ asymptote.

Spectroscopic parameters of the bound $^1\Sigma_0^+$ state are calculated by numerically solving the Schrödinger equation for nuclear wave functions expressed in the sinc-DVR basis⁴⁹, and the results are summarized in Table I. Our calculated results are compared with experimental results in literature^{32,50?}, with a satisfactory agreement.

B. Core-excited states

The $3d \rightarrow 4p$ core-to-valence excitation yields the Br 2D state corresponding to the $[3d^9][4p^6]$ configuration. The top panels in Figs. 1(a,b) show spin-orbit-free and

spin-orbit-coupled potential energy curves of the core-excited states. The H(2S)+Br(2D) asymptote gives rise to six molecular states, i.e., $^1\Sigma^+$, $^3\Sigma^+$, $^1\Pi$, $^3\Pi$, $^1\Delta$, and $^3\Delta$. Unlike the valence states, the six spin-orbit-free core-excited states are all degenerate (Fig. 1(a)). The Pauli repulsion between the fully occupied Br-4 p and the H-1 s shells results in the dissociative curves. Two other core excited configurations, $[3d^9][\sigma^2\pi^3\sigma^{*2}]$ and $[3d^9][\sigma^1\pi^4\sigma^{*2}]$, correlate with the counter-electronegative ionic H⁻+Br⁺ asymptote; they are located way above the energy window of the $3d \rightarrow 4p$ excitation.

The effect of spin-orbit coupling in the core-excited states is straightforward; it only splits the potential energy curves into two groups, correlating with the Br $^2D_{5/2}$ and $^2D_{3/2}$ states at the dissociation asymptote, respectively. The inset in Fig. 1(b) shows the average energy difference between the two spin-orbit states. The spin-orbit splitting is 1.06 eV at $R = 1.40$ Å, which differs only marginally from the value at the asymptotic limit (= 1.05 eV). The constant spin-orbit splitting manifests the inertness of the $3d$ shell in the H-Br interaction, as a core shell should be.

C. Core-to-valence absorption spectra

The core-to-valence absorption signals from the five valence states ($^1\Sigma_0^+$, $^3\Pi_1$, $^1\Pi_1$, $^3\Pi_0^+$, $^3\Sigma_1$) are calculated using the SO-GMC-QDPT results (Fig. 2). These states are involved in the UV photolysis of HBr²⁸⁻³⁰, and their bond-length dependent absorption spectra are of direct experimental interest. The absorption signals are constructed by taking a sum of oscillator strengths convoluted with Gaussian broadening of 150 meV, which mimics the finite lifetime of the core-excited states before their autoionizations. Note that core-to-valence excitations into the Rydberg series, i.e., $3d \rightarrow np$ ($n > 4$), which are of higher energies and have lower intensities,^{23,48,51,52} are of less interest and are hence not included in the present calculations.

The transition energies from the ground $^1\Sigma_0^+$ state (Fig. 2(a)) exhibits a sharp decrease as the internuclear distance increases. This is because the ground state is bound whereas the core-excited states are dissociative, and a small change in the internuclear distance strongly affects the transition energies. This feature allows for one-to-one mapping between the internuclear distance and the transition energy, which can be utilized for time-domain characterization of bound-state wavepacket motions^{9,10,20}.

Three of the lowest excited states, $^3\Pi_1$, $^1\Pi_1$, and $^3\Pi_0^+$ (Figs. 2(b)-(d)), do not show strong dependence on the internuclear distance in their transition energies, whereas the highest $^3\Sigma_1$ state shows a sharp increase, which is opposite to the trend in the ground $^1\Sigma_0^+$ state. All these trends are predictable based on the change in the bond order before and after the Br-3 d excitation. In the $^3\Pi$ and $^1\Pi$ states, an electron is excited from the non-bonding

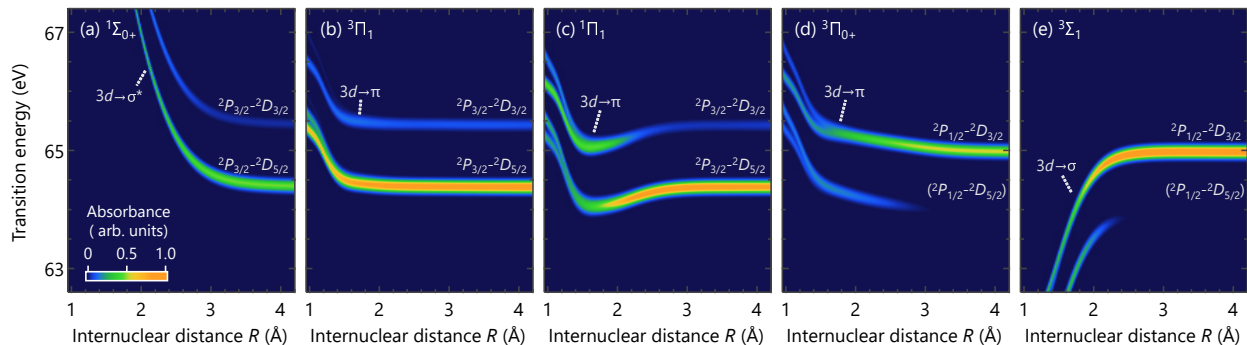


FIG. 2. The core-to-valence absorption strengths of HBr as a function of the internuclear distance calculated using the SO-GMC-QDPT method. The absorption strengths are computed from (a) $^1\Sigma_{0+}$, (b) $^3\Pi_1$, (c) $^1\Pi_1$, (d) $^3\Pi_{0+}$, and (e) $^3\Sigma_1$. In the asymptotic limit, the core-to-valence transitions converge to the atomic Br $^2P\text{-}^2D$ transitions, and the labels are given in each state. The $^2P_{1/2}\text{-}^2D_{5/2}$ transition is forbidden by the dipole selection rule in spherical symmetry, and the absorption associated with this transition fades away as the internuclear distance increases.

$3d$ orbitals into the non-bonding π orbital. Without a change in the bond order, the energy gaps between the valence states and the core-excited states are largely invariant with respect to the internuclear distance. The $^3\Sigma^+$ state is probed through $3d \rightarrow \sigma$ transition, in which process the bond order increases. The core-excited potentials, therefore, become less repulsive than the $^3\Sigma^+$ state, and resulting in the increasing behavior of the transition energy.

A remarkable behavior is observed in $^3\Pi_{0+}$ and $^3\Sigma_1$, the states correlating with the Br $^2P_{1/2}$ asymptote: the lower absorption signal disappears as the system approaches the asymptotic limit. The disappearance of the absorption signals is a clear manifestation of the change (and hence the selection rule) from molecular symmetry to the atomic symmetry. The lower absorption signal correspond to the $^2P_{1/2} \rightarrow ^2D_{5/2}$ transition in the asymptotic limit, which is prohibited by the atomic selection rule $\Delta J = 0, \pm 1$. When the two atoms are close to each other, however, Ω becomes a good quantum number instead of J , and the relaxed molecular selection rule ($\Delta\Omega = 0, \pm 1$) allows for the associated core-to-valence transitions. A fundamental question, at which internuclear distance two atoms recognize each other and start to behave as one molecule, can be tested by the appearance of the atomic-forbidden core-to-valence transitions.

IV. IONIC ELECTRONIC STATES

Next we will discuss the valence and core-excited states of HBr^+ . The singly-charged ion exhibits both bound and predissociative states, and we will discuss the Br- $3d$ edge probing of these electronic states.

A. Valence states

Figures 3(a) and (b) show spin-orbit-free and spin-orbit-coupled potential energy curves of HBr^+ , respectively. The atomic Br^+ that belongs to the $[3d^{10}][4p^4]$ configuration gives rise to three atomic states, 3P , 1D , and 1S . The ground X $^2\Pi$ state belongs to the $[\sigma^2\pi^3\sigma^*0]$ electronic configuration, and it correlates with the H (2S)+ Br^+ (3P) asymptote. There are three dissociative states, $^4\Sigma^-$, $^2\Sigma^-$, and $^4\Pi$, which also correlate with the H (2S)+ Br^+ (3P) asymptote. The main electronic configurations are $[\sigma^2\pi^2\sigma^*1]$ for $^4\Sigma^-$ and $^2\Sigma^-$, and $[\sigma^1\pi^3\sigma^*1]$ for $^4\Pi$. The excited A $^2\Sigma^+$ state arises from the H(2S)+ Br^+ (1D) asymptote, and the main electronic configuration is $[\sigma^1\pi^4\sigma^*0]$. Spin-orbit coupling splits the ground X $^2\Pi$ state into $^2\Pi_{3/2}$ and $^2\Pi_{1/2}$, and the excited A $^2\Sigma^+$ state becomes predissociative through an avoided crossing formed with the neighboring $^4\Sigma^-$, $^2\Sigma^-$, and $^4\Pi$ states^{34–36}.

Spectroscopic parameters calculated for the X $^2\Pi_{3/2}$, X $^2\Pi_{1/2}$, and A $^2\Sigma_{1/2}$ states are summarized in Table I. Overall, a good agreement with the experimental values^{32,34,50} is obtained, corroborating the accuracy of the present computational method.

B. Core-excited states

There are both bound and dissociative states in the core-excited configurations of HBr^+ (upper panels in Fig. 3), which contrasts with the neutral system where only dissociative states are formed. The three lowest spin-orbit-free states, $^2\Delta$, $^2\Pi$, and $^2\Sigma^+$, belong to the $[3d^9][\sigma^2\pi^4\sigma^*0]$ configuration, and they all have a potential shape that looks similar to the valence ground X $^2\Pi$ state (Table I). This is not surprising since the $3d \rightarrow \pi$ excitation is a nonbonding-to-nonbonding transition. It does not alter the bond order, and a similar H-Br bonding

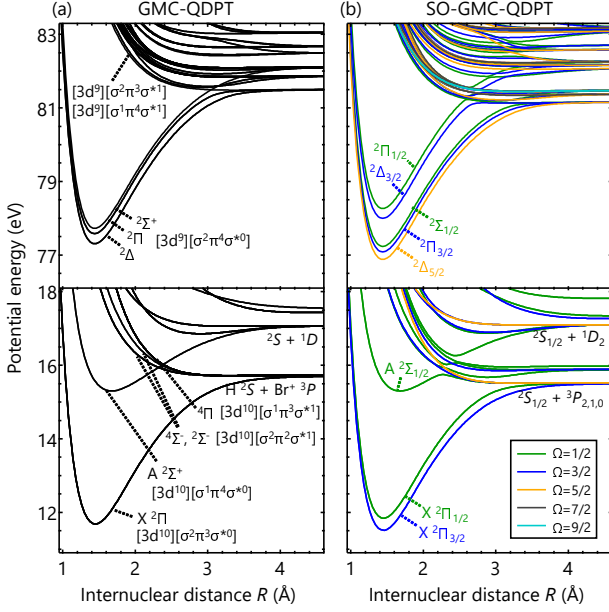


FIG. 3. Potential energy curves of HBr^+ as a function of the internuclear distance R obtained from calculations (a) without and (b) with spin-orbit coupling. The lower panels show the valence states, and the upper panels show the Br-3d core excited states. In the asymptotic limits the atomic term symbols are given for some states in the lower panels. For the spin-orbit-coupled states, different colors are used to indicate their associated Ω quantum numbers. The inset in (b) shows average spin-orbit splittings in the ${}^2\Pi$ and the ${}^2\Delta$ states.

interaction follows. The dissociative core-excited states are formed by the contributions from the $[3d^9][\sigma^2\pi^3\sigma^*1]$ and $[3d^9][\sigma^1\pi^3\sigma^*1]$ configurations, wherein the antibonding σ^* orbital is singly occupied. Their dissociative character is similar to that of the neutral core-excited states. However, the larger number of configurations allowed in the ionic system congests the potential energy curves, making those states less useful for valence-state probing.

One thing that draws attention is that the three bound states are energetically separated, whereas in the neutral system all six spin-orbit-free core-excited states are degenerate. The origin of the energy splitting can be understood in terms of the ligand-field splitting^{53–58}. In the ionic system, there is a field gradient along the bonding axis which works on the Br-3d orbitals. The ligand fields are mainly created by two contributions. One is the polarized density of the valence Br-4p electrons (valence term) distributed between the parallel ($4p_z$) and perpendicular ($4p_{x,y}$) directions to the bond axis. The polarized electron density is measured by $\rho = n_{p_z} - (n_{p_x} + n_{p_y})/2$. Formally, $\rho = 0$ in the neutral core-excited states, and $\rho = 1$ for the ionic core-excited states. The other is due to the partial charge on the surrounding atoms (point-charge term). In the present case, the partial charge can be on the H atom, even though this contribution is expected to be small since the covalent σ orbital is fully

occupied. The ligand fields unfold the degeneracy of the Br-3d orbitals through the Stark effect. The states with the hole (which can be viewed as an effective positive charge) pointing away from the proton are lower in energy larger, resulting in the ascending energy ordering from ${}^2\Delta$ to ${}^2\Pi$, and to ${}^2\Sigma$.

The effects of spin-orbit coupling in the $[3d^9][\sigma^2\pi^4\sigma^*0]$ configuration is expected to be atom-like as in the case of the neutral system, since the orbital angular momentum originates solely from the Br-3d core hole. However, care must be taken in analyzing the energy splittings because the effects of spin-orbit coupling and the ligand-field splitting are entangled. In order to analyze the two interactions separately, we employ a model Hamiltonian

$$\begin{aligned} \hat{H} = & \hat{H}_0 + C_2^0 [3\hat{L}_z^2 - \hat{L}(\hat{L} + 1)] \\ & + C_4^0 [35\hat{L}_z^4 - 30\hat{L}(\hat{L} + 1)\hat{L}_z^2 \\ & + 25\hat{L}_z^2 - 6\hat{L}(\hat{L} + 1) + 3\hat{L}^2(\hat{L} + 1)^2] \\ & + \lambda[(1/2)(\hat{L}_- \hat{S}_+ + \hat{L}_+ \hat{S}_-) + \hat{L}_z \hat{S}_z], \quad (1) \end{aligned}$$

which describes the spin-orbit coupling and the ligand-field splitting as additional effects to the Br-3d core-ionized states. In Eq. (1), the operator \hat{H}_0 is the Hamiltonian for the Br-3d ionized states, \hat{L} , \hat{L}_z , and \hat{L}_\pm are orbital angular momentum operators, and \hat{S} , \hat{S}_z , and \hat{S}_\pm are spin momentum operators. The parameters C_2^0 and C_4^0 represent the noncubic and cubic ligand-field strengths, respectively, and λ is the spin-orbit coupling constant for the Br-3d orbitals. By performing least-square fittings of the calculated state energies to the eigenvalues of the model Hamiltonian (see refs^{59,7} for details), the perturbation-free energy E_{3d} as well as the field parameters can be extracted.

Figure 4 summarizes the model parameters determined from 0.8 Å to 2.4 Å. The field-free energy E_{3d} (Fig. 4(a)) exhibits bound-potential shape corresponding to the bonding $[\sigma^2\pi^4\sigma^*0]$ valence configuration. The spin-orbit coupling constant (Fig. 4(b)) is nearly invariant, being around 0.42 eV even when the internuclear distance is so short that the shape of the $3d_{z^2}$ orbital is deformed. The ligand-field parameters (Figs. 4(c,d)), in contrast, show sharp increases at the shorter internuclear distance. In general, the valence term contributes to C_2^0 , and the point-charge term contributes to both C_2^0 and C_4^0 . The sharp increase observed at shorter internuclear distance in both C_2^0 and C_4^0 is attributed to the point-charge term, and the finite value that remains at $R > 1.2$ Å in C_2^0 is due to the valence term. The values determined previously based on photoelectron spectroscopic data are $C_2^0 = 27.0$ meV and $\lambda = 0.416$ eV⁵⁶, and the present results are in a good agreement showing $C_2^0 = 32.7$ meV and $\lambda = 0.420$ eV at $R = 1.4$ Å. The results here indicate that the C_4^0 term is almost negligible, being less than 0.5 meV at $R > 1.4$ Å.

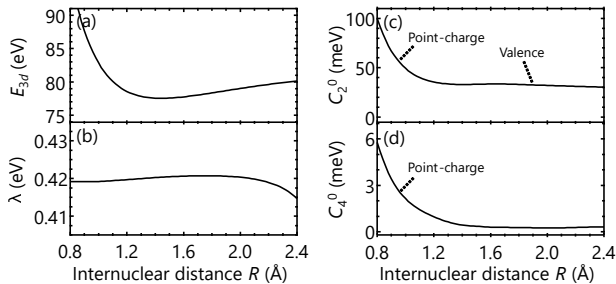


FIG. 4. Fitted results of (a) the field-free energy E_{3d} , (b) the spin-orbit coupling constant λ , (c) the noncubic ligand-field parameter C_0^2 , and (d) the cubic ligand-field parameter C_0^4 . The spin-orbit coupling constant is nearly invariant with respect to the internuclear distance. The sharp increases observed both in the noncubic and cubic ligand-field parameters are attributed to the point-charge contribution from H atom. The finite value remaining in the noncubic field parameter at $R > 1.2$ Å is attributed to the polarized density of the valence Br-4p electrons.

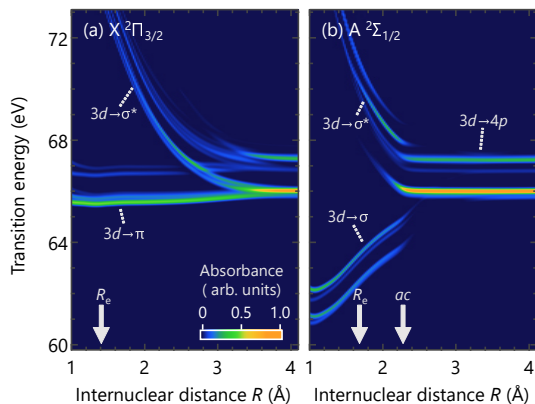


FIG. 5. Core-to-valence absorption spectra of (a) $X^2\Pi_{3/2}$ and (b) $A^2\Sigma_{1/2}$ states as a function of the internuclear distance calculated using the SO-GMC-QDPT results. The equilibrium internuclear distances as well as the location of the avoided crossing are indicated on the horizontal axis by white arrows.

C. Core-to-valence absorption spectra

Figure 4(a) shows the core-to-valence absorption strengths calculated from the bound $X^2\Pi_{3/2}$ state. In the vicinity of the equilibrium geometry ($R_e = 1.45$ Å), the lower absorption signals that correspond to the $3d \rightarrow \pi$ transitions are nearly invariant with respect to the internuclear distance. This trend is expected from the parallel relation between the valence and the core-excited potentials. On the other hand, the upper absorption signals corresponding to $3d \rightarrow \sigma^*$ transitions show a strong dependence on the internuclear distance, which will be useful in tracking the vibrational motions induced in the ionic ground state.

Figure 5(b) shows the core-to-valence absorption spectra calculated from the predissociative $A^2\Sigma_{1/2}$ state. One can clearly observe drastic variation of the absorption signals which is occurring around the avoided crossing ($R \sim 2.3$ Å). In the bound-potential region ($R_e = 1.68$ Å), the electronic state belongs to the $[3d^{10}][\sigma^1\pi^4\sigma^{*0}]$ configuration, and the population therein is probed by the $3d \rightarrow \sigma$ or $3d \rightarrow \sigma^*$ transitions. These are the transitions into the bonding or antibonding molecular orbitals, thus resulting in the large internuclear dependence of the transition energies. At the avoided crossing, electronic-state characters are exchanged, and the main electronic configuration contributing to the outer dissociative part of the potential becomes $[3d^{10}][\sigma^2\pi^2\sigma^{*1}]$ and $[3d^{10}][\sigma^1\pi^3\sigma^{*1}]$. The state after the avoided crossing, therefore, will be probed by the $3d \rightarrow \sigma$ and $3d \rightarrow \pi$ transitions, which are more properly described as $3d \rightarrow 4p$ atomic transitions at the elongated internuclear distance. The sudden increase in the absorption intensities also reflects the atomic nature of the transitions. One might notice that the signal convergence to the atomic lines occurs at shorter internuclear distance on the A state (~ 2.3 Å) than on the X state (~ 3.6 Å). The difference indicates the short-range nature of the orbital interactions in the $[3d^{10}][\sigma^2\pi^2\sigma^{*1}]$ and $[3d^{10}][\sigma^1\pi^3\sigma^{*1}]$ configurations, wherein the antibonding σ^* orbital is singly occupied. The findings here demonstrate the strong capability of the core-level absorption spectroscopy to directly probe nonadiabatic molecular dynamics. This is enabled by the fact that the core orbitals are largely invariant throughout the whole reaction coordinates and the absorption reflects only the variations in the valence states.

V. COMPARISON WITH EXPERIMENTAL TRANSIENT-ABSORPTION SPECTRUM

In order to evaluate the accuracy of the calculated core-excited potentials, core-to-valence absorption spectra are simulated by numerically solving the time-dependent Schrödinger equation^{60,61}, and a comparison is made to an experimental XUV absorption spectrum. The valence electronic states selected for the simulations are the neutral $X^1\Sigma_0^+$ state and the ionic $X^2\Pi_{3/2}$ and $^2\Pi_{1/2}$ states. The initial wave functions are taken to be in the ground vibrational state of each electronic state, and the lifetime of the core-excited states are set to be $T = 4.4$ fs, corresponding to the spectral width of $\Gamma = 150$ meV. The time propagation of the non-Hermitian Hamiltonian is performed using the short-iterative Arnoldi method⁶². The experimental absorption spectrum is measured using the HHG-based attosecond XUV beamline in Berkeley^{63,64}. The change in absorption signals following strong-field ionization are recored as optical density (ΔOD), which is the difference in the absorbance measured with and without the ionizing pump pulse. Positive ΔOD corresponds to ionized-state absorption from HBr^+ , and nega-

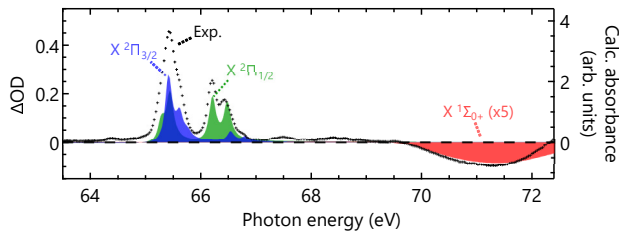


FIG. 6. Comparison of the simulated and the experimental transient absorption spectra. The experimental spectra of HBr and HBr^+ (cross marks, left axis) are recorded as optical density difference (ΔOD), which is the difference in absorbance when the ionizing laser pulse is on and off. The spectra are averaged over a delay range from 20 fs to 90 fs. Positive ΔOD corresponds to ionized-state absorption, and negative ΔOD corresponds to ground-state bleach. The simulated absorption spectra (filled areas, right axis) are obtained by numerically solving the time-dependent Schrödinger equation for nuclear wave packets prepared on the valence and core-excited potentials. A good agreement is observed between the experimental and the simulated spectra.

tive ΔOD corresponds to ground-state bleach in the neutral HBr.

Figure 6 shows the simulated and the experimental core-to-valence absorption spectra. Note that the simulated signals from the neutral $X\ ^1\Sigma_0^+$ state are magnified five times and the sign is flipped for better visualization. Overall, an excellent agreement is seen both for the neutral and ionic signals, corroborating the capabilities of the computational method. The deviation seen from the neutral X state above 72 eV is due to the positive $3d \rightarrow \sigma^*$ absorption signals from the ionic $X\ ^2\Pi$ states, which are not included in the present simulation.

Even though the neutral ground state and the ionic ground states have similar potential shapes, their appearances on the core-to-valence absorption spectra are markedly different. The neutral $X\ ^1\Sigma_0^+$ state exhibits a broad absorption feature centered at 71.3 eV, and its spectral width is too broad for the spin-orbit splitting to be resolved. The broadening effect is due to the motion of the nuclear wave packets on the dissociative core-excited potentials reached after $3d \rightarrow \sigma^*$ transition. On the other hand, the ionic $X\ ^2\Pi$ states probed through $3d \rightarrow \sigma^*$ transitions show sharp absorption features, and the spin-orbit (the yellow vs. the green bands and the far separated peaks within each band) and the ligand-field splittings (the peaks within each band with intervals < 0.1 eV) are well resolved. Due to the parallel potential energy curves of the relevant valence and core-excited states, the splittings do not originate from vibronic progression. Spectral broadening from nuclear motion is hence insignificant. The contrasting core-to-valence absorption profiles of HBr and HBr^+ demonstrate the importance of accounting for the shapes of core-excited potentials.

VI. CONCLUSIONS

We have applied the SO-GMC-QDPT method to calculate the Br- $3d$ core-to-valence absorption signals in HBr and HBr^+ . In the neutral HBr, five valence states involved in the UV photolysis are investigated. The trends in the transition energies with respect to the internuclear distance are understood based on the change in the bond order before and after the core-to-valence excitation. The disappearance of the absorption signals observed in the states correlated with the Br $^2P_{1/2}$ asymptote is remarkable, for it directly reflecting the change of the state symmetries from molecular to atomic. In the ionic HBr^+ , the core-to-valence absorption signals are calculated from the bound X state and the predissociative A state. The signature of the system evolving across the avoided crossing is found to be manifested as the disappearance of drifting $3d \rightarrow \sigma$ and $3d \rightarrow \sigma^*$ signals and the appearance of the converged $3d \rightarrow 4p$ atomic lines. A comparison is made between the simulated and experimental spectra for the neutral and ionic ground states, which exhibits an excellent agreement. The peak broadening effects due to the nuclear wave-packet motion are demonstrated to be critical for the neutral $3d \rightarrow \sigma^*$ signals. With the good theory-experiment agreements in the present work, we foresee that the SO-GMC-QDPT method will be a versatile tool for calculating core-excited electronic structures.

ACKNOWLEDGMENTS

Y.K., D.M.N., and S.R.L. acknowledge the US Army Research Office (ARO) (No. W911NF-14-1-0383). Y.K. and S.R.L. also acknowledge the National Science Foundation (NSF) (No. CHE-1660417). T.Z. acknowledges the Natural Sciences and Engineering Research Council (NSERC) of Canada for research funding (No. RGPIN-2016-06276), and also Carleton University for start-up Grant (No. 186853). Part of the computations were performed using workstations at the Molecular Graphics and Computation Facility (MGCF) at UC Berkeley, which is funded by the National Institutes of Health (NIH) (No. S10OD023532). Y.K. acknowledges financial support by the Funai Overseas Scholarship.

¹S. R. Leone and D. M. Neumark, *Faraday Discuss.* **194**, 15 (2016).

²P. M. Kraus, M. Zürich, S. K. Cushing, D. M. Neumark, and S. R. Leone, *Nature Reviews Chemistry* **2**, 82 (2018).

³P. B. Corkum, *Phys. Rev. Lett.* **71**, 1994 (1993).

⁴F. Krausz and M. Ivanov, *Rev. Mod. Phys.* **81**, 163 (2009).

⁵L. Gallmann, C. Cirelli, and U. Keller, *Annual Review of Physical Chemistry* **63**, 447 (2012).

⁶Z. Chang, P. B. Corkum, and S. R. Leone, *J. Opt. Soc. Am. B* **33**, 1081 (2016).

⁷E. Goulielmakis, Z.-H. Loh, A. Wirth, R. Santra, N. Rohringer, V. S. Yakovlev, S. Zherebtsov, T. Pfeifer, A. M. Azzeer, M. F. Kling, S. R. Leone, and F. Krausz, *Nature* **466**, 739 (2010).

⁸Y. Kobayashi, M. Reduzzi, K. F. Chang, H. Timmers, D. M. Neumark, and S. R. Leone, *Phys. Rev. Lett.* **120**, 233201 (2018).

⁹E. R. Hosler and S. R. Leone, *Phys. Rev. A* **88**, 023420 (2013).

- ¹⁰Z. Wei, J. Li, L. Wang, S. T. See, M. H. Jhon, Y. Zhang, F. Shi, M. Yang, and Z.-H. Loh, *Nature Communications* **8**, 735 (2017).
- ¹¹L. Drescher, M. C. E. Galbraith, G. Reitsma, J. Dura, N. Zavoronkov, S. Patchkovskii, M. J. J. Vrakking, and J. Mikosch, *The Journal of Chemical Physics* **145**, 011101 (2016).
- ¹²A. S. Chatterley, F. Lackner, C. D. Pemmaraju, D. M. Neumark, S. R. Leone, and O. Gessner, *The Journal of Physical Chemistry A* **120**, 9509 (2016).
- ¹³Y. Pertot, C. Schmidt, M. Matthews, A. Chauvet, M. Huppert, V. Svoboda, A. von Conta, A. Tehlar, D. Baykusheva, J.-P. Wolf, and H. J. Wörner, *Science* **355**, 264 (2017).
- ¹⁴A. R. Attar, A. Bhattacharjee, C. D. Pemmaraju, K. Schnorr, K. D. Closser, D. Prendergast, and S. R. Leone, *Science* **356**, 54 (2017).
- ¹⁵M. Schultze, K. Ramasesha, C. Pemmaraju, S. Sato, D. Whitmore, A. Gandman, J. S. Prell, L. J. Borja, D. Prendergast, K. Yabana, D. M. Neumark, and S. R. Leone, *Science* **346**, 1348 (2014).
- ¹⁶M. Lucchini, S. A. Sato, A. Ludwig, J. Herrmann, M. Volkov, L. Kasmi, Y. Shinohara, K. Yabana, L. Gallmann, and U. Keller, *Science* **353**, 916 (2016).
- ¹⁷M. Zürch, H.-T. Chang, L. J. Borja, P. M. Kraus, S. K. Cushing, A. Gandman, C. J. Kaplan, M. H. Oh, J. S. Prell, D. Prendergast, C. D. Pemmaraju, D. M. Neumark, and S. R. Leone, *Nature Communications* **8**, 15734 (2017).
- ¹⁸L. M. Carneiro, S. K. Cushing, C. Liu, Y. Su, P. Yang, A. P. Alivisatos, and S. R. Leone, *Nature Materials* **16**, 819 (2017).
- ¹⁹Y. Zhang, W. Hua, K. Bennett, and S. Mukamel, "Nonlinear spectroscopy of core and valence excitations using short x-ray pulses: Simulation challenges," in *Density-Functional Methods for Excited States*, edited by N. Ferré, M. Filatov, and M. Huix-Rotllant (Springer International Publishing, Cham, 2016) pp. 273-345.
- ²⁰A. D. Dutoi and S. R. Leone, *Chemical Physics* **482**, 249 (2017).
- ²¹A. P. Bazante, A. Perera, and R. J. Bartlett, *Chemical Physics Letters* **683**, 68 (2017).
- ²²I. Corral, J. Gonzalez-Vzquez, and F. Martn, *Journal of Chemical Theory and Computation* **13**, 1723 (2017), pMID: 28240892.
- ²³A. Cummings and G. O'Sullivan, *Phys. Rev. A* **54**, 323 (1996).
- ²⁴Z.-H. Loh and S. R. Leone, *The Journal of Chemical Physics* **128**, 204302 (2008).
- ²⁵M.-F. Lin, D. M. Neumark, O. Gessner, and S. R. Leone, *The Journal of Chemical Physics* **140**, 064311 (2014).
- ²⁶A. R. Attar, L. Piticco, and S. R. Leone, *The Journal of Chemical Physics* **141**, 164308 (2014).
- ²⁷A. S. Chatterley, F. Lackner, D. M. Neumark, S. R. Leone, and O. Gessner, *Phys. Chem. Chem. Phys.* **18**, 14644 (2016).
- ²⁸P. M. Regan, S. R. Langford, A. J. Orr-Ewing, and M. N. R. Ashfold, *The Journal of Chemical Physics* **110**, 281 (1999).
- ²⁹A. G. Smolin, O. S. Vasyutinskii, G. G. Balint-Kurti, and A. Brown, *The Journal of Physical Chemistry A* **110**, 5371 (2006).
- ³⁰R. Valero, D. G. Truhlar, and A. W. Jasper, *The Journal of Physical Chemistry A* **112**, 5756 (2008).
- ³¹J. Delwiche, P. Natalis, J. Momigny, and J. Collin, *Journal of Electron Spectroscopy and Related Phenomena* **1**, 219 (1972).
- ³²A. Banichevich, R. Klotz, and S. Peyerimhoff, *Molecular Physics* **75**, 173 (1992).
- ³³R. F. Barrow and A. D. Caunt, *Proceedings of the Physical Society. Section A* **66**, 617 (1953).
- ³⁴P. Baltzer, M. Larsson, L. Karlsson, M. Lundqvist, and B. Wannberg, *Phys. Rev. A* **49**, 737 (1994).
- ³⁵A. Mank, T. Nguyen, J. D. D. Martin, and J. W. Hepburn, *Phys. Rev. A* **51**, R1 (1995).
- ³⁶M. Penno, A. Holzwarth, and K.-M. Weitzel, *The Journal of Physical Chemistry A* **102**, 1927 (1998).
- ³⁷T. Zeng, *The Journal of Chemical Physics* **146**, 144103 (2017).
- ³⁸H. Nakano, R. Uchiyama, and K. Hirao, *Journal of Computational Chemistry* **23**, 1166 (2002).
- ³⁹M. Miyajima, Y. Watanabe, and H. Nakano, *The Journal of Chemical Physics* **124**, 044101 (2006).
- ⁴⁰R. Ebisuzaki, Y. Watanabe, and H. Nakano, *Chemical Physics Letters* **442**, 164 (2007).
- ⁴¹M. W. Schmidt, K. K. Baldrige, J. A. Boatz, S. T. Elbert, M. S. Gordon, J. H. Jensen, S. Koseki, N. Matsunaga, K. A. Nguyen, S. Su, T. L. Windus, M. Dupuis, and J. A. Montgomery, *Journal of Computational Chemistry* **14**, 1347 (1993).
- ⁴²T. Zeng, D. G. Fedorov, and M. Klobukowski, *The Journal of Chemical Physics* **131**, 124109 (2009).
- ⁴³T. Zeng, D. G. Fedorov, and M. Klobukowski, *The Journal of Chemical Physics* **132**, 074102 (2010).
- ⁴⁴T. Zeng, D. G. Fedorov, and M. Klobukowski, *The Journal of Chemical Physics* **133**, 114107 (2010).
- ⁴⁵T. Zeng, D. G. Fedorov, and M. Klobukowski, *The Journal of Chemical Physics* **134**, 024108 (2011).
- ⁴⁶Y.-K. Choe, H. A. Witek, J. P. Finley, and K. Hirao, *The Journal of Chemical Physics* **114**, 3913 (2001).
- ⁴⁷H. A. Witek, Y.-K. Choe, J. P. Finley, and K. Hirao, *Journal of Computational Chemistry* **23**, 957 (2003).
- ⁴⁸L. Nahon, P. Morin, and F. C. Farnoux, *Physica Scripta* **1992**, 104 (1992).
- ⁴⁹D. T. Colbert and W. H. Miller, *The Journal of Chemical Physics* **96**, 1982 (1992).
- ⁵⁰A. Yench, A. Cormack, R. Donovan, K. Lawley, A. Hopkirk, and G. King, *Chemical Physics* **238**, 133 (1998).
- ⁵¹P. Morin and I. Nenner, *Phys. Rev. Lett.* **56**, 1913 (1986).
- ⁵²Y. F. Hu, G. M. Bancroft, J. Karvonen, E. Nommiste, A. Kivimäki, H. Aksela, S. Aksela, and Z. F. Liu, *Phys. Rev. A* **56**, R3342 (1997).
- ⁵³G. M. Bancroft and J. S. Tse, *Comments on Inorganic Chemistry* **5**, 89 (1986).
- ⁵⁴J. N. Cutler, G. M. Bancroft, and K. H. Tan, *The Journal of Chemical Physics* **97**, 7932 (1992).
- ⁵⁵D. Sutherland, Z. Liu, G. Bancroft, and K. Tan, *Nuclear Instruments and Methods in Physics Research Section B: Beam Interactions with Materials and Atoms* **87**, 183 (1994).
- ⁵⁶Z. Liu, G. Bancroft, K. Tan, and M. Schachter, *Journal of Electron Spectroscopy and Related Phenomena* **67**, 299 (1994).
- ⁵⁷R. Puttner, M. Domke, K. Schulz, A. Gutierrez, and G. Kaindl, *Journal of Physics B: Atomic, Molecular and Optical Physics* **28**, 2425 (1995).
- ⁵⁸J. Johnson, J. N. Cutler, G. M. Bancroft, Y. F. Hu, and K. H. Tan, *Journal of Physics B: Atomic, Molecular and Optical Physics* **30**, 4899 (1997).
- ⁵⁹G. M. Bancroft, D. K. Creber, and H. Basch, *The Journal of Chemical Physics* **67**, 4891 (1977).
- ⁶⁰A. Nikodem, R. D. Levine, and F. Remacle, *The Journal of Physical Chemistry A* **120**, 3343 (2016), pMID: 26928262.
- ⁶¹S. van den Wildenberg, B. Mignolet, R. D. Levine, and F. Remacle, *Phys. Chem. Chem. Phys.* **19**, 19837 (2017).
- ⁶²W. T. Pollard and R. A. Friesner, *The Journal of Chemical Physics* **100**, 5054 (1994).
- ⁶³H. Timmers, M. Sabbar, J. Hellwagner, Y. Kobayashi, D. M. Neumark, and S. R. Leone, *Optica* **3**, 707 (2016).
- ⁶⁴H. Timmers, Y. Kobayashi, K. F. Chang, M. Reduzzi, D. M. Neumark, and S. R. Leone, *Opt. Lett.* **42**, 811 (2017).